IEEE Open Journal of Vehicular Technology

Received 2 March 2026; accepted 9 April 2026. Date of publication 16 April 2026;
date of current version 30 April 2026. The review of this article was coordinated by Editor José Rodríguez-Piñeiro.

Digital Object Identifier 10.1109/OJVT.2026.3683456

Channel Estimation Assisted Bistatic Localization in Terrestrial and Non-Terrestrial Networks

KUNLUN LI (Member, IEEE), CHAO ZHANG (Member, IEEE), MOHAMMED EL-HAJJAR (Senior Member, IEEE), CHAO XU (Senior Member, IEEE), AND LAJOS HANZO (Life Fellow, IEEE)

School of Electronics and Computer Science, University of Southampton, SO17 1BJ Southampton, U.K.

CORRESPONDING AUTHOR: LAJOS HANZO (e-mail: lh@ecs.soton.ac.uk).

This work was supported in part by Engineering and Physical Sciences Research Council (EPSRC), in part by the Platform for Driving Ultimate Connectivity (TITAN) under Grant EP/X04047X/1 and Grant EP/Y037243/1, in part by Robust and Reliable Quantum Computing (RoaRQ) under Grant EP/W032635/1, in part by PerCom under Grant EP/X012301/1, and in part by India-U.K. Intelligent Spectrum Innovation ICON under Grant UKRI-1859.

ABSTRACT Low-Earth-orbit (LEO) satellites are regarded as a key enabler for 6G communications and localization, due to their large coverage beyond conventional terrestrial networks. In this paper, we propose a downlink LEO base station (BS) bistatic localization framework relying on hybrid beamforming that alleviates the reliance on ultra-fine angle estimation by jointly exploiting time-frequency-spatial observations. A multiple-measurement-vector (MMV) based sparse model is constructed for attaining accurate channel gains and angles from limited pilots and moderate array sizes, where a modified block orthogonal matching pursuit (BOMP) algorithm is proposed to enhance robustness under highly correlated sensing matrices for localization purposes. After geometry-based timing-advance and Doppler pre-compensation at the BS, a two-dimensional (2D) upsampling matched filter having fine delay-Doppler grids is applied to estimate the residual time of arrival (ToA) and Doppler frequency. Then, the final user equipment (UE) position is obtained by intersecting the BS-centered angle-of-arrival (AoA) ray with a bistatic-range ellipse derived from the residual delay. The numerical results under realistic LEO-BS bistatic scenarios demonstrate that the proposed scheme achieves meter-level localization accuracy and highlight the performance gains attained by increasing the number of pilot symbols, subcarriers, and angular resolutions.

INDEX TERMS Localization/positioning, channel estimation, low Earth orbit, non-terrestrial network.

NOMENCLATURE

AMP	Approximate message passing.
AoA	Angle-of-arrival.
AoD	Angle-of-departure.
AWGN	Additive white Gaussian noise.
BOMP	Block orthogonal matching pursuit.
BS	Base station.
CE	Channel estimation.
CoSaMP	Compressive sampling matching pursuit.
CSI	Channel state information.
DL	Downlink.
DPC	Doppler pre-compensation.
EIRP	Effective isotropic radiated power.
GNSS	Global navigation satellite system.
IoT	Internet of things.
ISAC	Integrated sensing and communications.
JRC	Joint radar communication.
LEO	Low-earth-orbit.
LMMSE	Linear minimum mean square error.
LoS	Line-of-sight.
MIMO	Multiple-input multiple-output.
MMV	Multiple measurement vector.
NLoS	Non-line-of-sight.
NR	New radio.
NTN	Non-terrestrial network.
OFDM	Orthogonal frequency division multiplexing.

OMP	Orthogonal matching pursuit.
OTFS	Orthogonal time frequency space.
RC	Receive combining.
RCS	Radar cross section.
RF	Radio frequency.
RIS	Reconfigurable intelligent surface.
RMSE	Root mean squared error.
RSMA	Rate splitting multiple access.
SAGIN	Space-air-ground-integrated networks.
SMV	Single measurement vector.
SNR	Signal-to-noise ratio.
TA	Timing advance.
TN	Terrestrial network.
ToA	Time-of-arrival.
TPC	Transmit precoding.
UE	User equipment.
UPA	Uniform planar array.

I. INTRODUCTION

As global communication demand escalates, conventional terrestrial networks (TN) face limitations in coverage, service reliability, and resource utilization, which require improvements for next-generation systems [1]. Non-terrestrial networks (NTN) relying on low-earth-orbit (LEO) satellites offer coverage, geometry and waveform reuse that complement terrestrial 6G systems [2], [3], [4]. Localization in 6G plays an important role in applications such as emergency services, logistics, and autonomous driving [5], [6]. While global navigation satellite systems (GNSS) serve as the gold standard for outdoor positioning with high accuracy in open-sky conditions, their performance degrades significantly in GNSS-challenged environments, such as deep urban canyons, indoors, or areas suffering from severe signal blockage [7]. In these scenarios, satellite visibility is often limited, and multi-path effects are severe. Consequently, LEO satellites, having high transmit power and dense constellations, offer a promising complementary solution [8].

The GNSS constellations are designed to ensure the simultaneous visibility of at least four satellites for trilateration [9]. LEO satellites might be viewed as a potential design alternative, but owing to their low altitude and high velocity, they exhibit a short service window for a specific user [10]. Nonetheless, exploiting angle-of-arrival (AoA) information alongside propagation delay is worth investigating in the context of instantaneous and single-satellite localization. In this case, the long propagation distance and substantial delay make precise positioning heavily reliant on high-accuracy angle estimates in the single-LEO satellite scenario, which is challenging for both signal processing and hardware, especially for the calibration of large arrays, phase noise mitigation, and synchronization [11], [12].

From a system perspective, recent surveys have established the architectural role of NTN in 6G, highlighting multi-layer space–air–ground integration, 3GPP standardization progress, and the benefits of LEO constellations in terms of latency and rate [13], [14], [15]. NTN-based 6G localization has been surveyed in [5], where the authors discuss how LEO satellites can provide favourable geometry and global visibility, while also identifying stringent synchronization, Doppler compensation, and joint TN–NTN design as key challenges. More broadly, ground–air–space localization has been treated in the tutorial [13], which provides a unified view of radio-based positioning across terrestrial, aerial, and satellite segments, quantifying the sensitivity of the localization accuracy to system geometry and signal design. Specifically, LEO-based sensing and localization has recently attracted much attention [5], [16], [17], [18], [19], [20], [21], [22]. In [16], satellite based Internet-of-Things (IoT) localization is achieved via joint Doppler and angle-of-arrival estimation. In [17], [18], methods are proposed to mitigate strong LEO-induced Doppler in 5G-NTN receivers. Blind Doppler tracking relying on broadcast orthogonal frequency division multiplexing (OFDM) LEO signals without a dedicated navigation payload has been demonstrated in [21]. Robust and risk-aware LEO beamforming under channel and position uncertainty has been investigated in [20], while the fundamentals and performance limits of LEO-based localization have been established in [22]. These works confirm that LEO-based localization is feasible, but they often assume high-quality angle estimates or rely on satellite-side processing having stringent hardware and calibration requirements.

Accurate channel estimation (CE) is vital for both high-throughput communication and precise positioning [23], [24], [25], [26], [27]. However, LEO channels are strongly time-varying and Doppler-dominated, which renders conventional pilot-based schemes inefficient. Massive multiple-input multiple-output (MIMO) OFDM channel estimation tailored to LEO satellite communications has been developed in [24], where a geometry-dependent wideband channel model is combined with a two-stage estimation framework that exploits the sparsity and structured time–frequency correlation of LEO channels. To deal with severe Doppler and time selectivity, orthogonal time frequency space (OTFS)-based LEO systems have been studied in [28], which proposes joint Bayesian channel estimation and data detection in the delay–Doppler domain. In the context of massive IoT, grant-free random access and user-activity detection combined with joint channel estimation have been conceived for LEO-enabled networks [25], where a message-passing-based algorithm leverages the sporadic and sparse nature of user activity. To mitigate channel aging and reduce pilot overhead, block-based Kalman channel tracking for LEO massive MIMO has been proposed in [29]. Furthermore, integrated sensing and communications (ISAC) frameworks have been developed in [19] for massive MIMO LEO, where the same waveform is exploited for both data transmission and parameter estimation. Overall, these works demonstrate that (i) exploiting the typical LEO propagation scenario (e.g., geometry, sparsity, and two-time-scale variations) and (ii) jointly designing communication and sensing functionalities are crucial for achieving robust CSI and high-accuracy positioning. Nevertheless, most

schemes are monostatic and satellite-centric, and they usually assume that fine angular resolution and sophisticated signal processing are available at the satellite or user terminals, which may not be practical for reasons of cost- and power-constraints.

To elaborate, bistatic and multistatic sensing has emerged as a powerful solution for exploiting the distributed nature of wireless networks [30]. Classical bistatic radar and localization frameworks provide fundamental insights into ellipse-based range geometry, synchronization, and target localization based on bistatic measurements. It has also been shown that terrestrial systems using OFDM based joint radar–communication (JRC) architectures and 5G NR-based sensing can be reused for range–Doppler estimation with the aid of appropriate synchronization and frame design [31]. Recent research on multistatic ISAC further exploited cooperation among multiple base stations or access points to enhance sensing coverage and robustness [32], [33], [34], [35]. For example, RIS-aided bistatic ISAC has been studied in [32], where a reconfigurable intelligent surface (RIS) supports a bistatic link between a communication transmitter and a separate sensing receiver, relying on low-cost components. Cellular-network-based multistatic ISAC architectures that reuse existing base-station deployments for cooperative sensing have been investigated in [33].

In the LEO context, bistatic ISAC frameworks exploiting separated radar receivers have been proposed in [34], [35], where rate-splitting multiple access (RSMA) is employed to manage interference, while satisfying demanding communication and sensing constraints. Space–air–ground integrated bistatic sensing architectures, have also been explored [36], in which LEO, aerial platforms, and terrestrial nodes jointly participate in sensing. Existing bistatic LEO investigations, however, largely focus on target detection and communication–sensing trade-offs, rather than on user-centric localization relying on TN–NTN cooperation.

Existing LEO localization studies are monostatic and satellite-centric [16], [19], [20], [21], [22], often assuming either fine angular resolution or sophisticated signal processing [11], [12]. The associated LEO channel estimation techniques tend to exploit sparsity and geometry but they do not readily allow the translation of the recovered parameters into a single-LEO satellite bistatic positioning pipeline, while obeying an explicit geometric constraint [24]. On the other hand, the bistatic/multistatic ISAC literature tends to focus mainly on the detection issues or on the sensing–communication trade-offs [34], rather than on user-centric localization under hybrid beamforming relying on symbol-by-symbol based projections. Given the above knowledge gaps, we intrinsically amalgamate LEO-specific channel estimation in the TN-NTN cooperation in the face of bistatic range-angle constraints in a unified localization architecture. In particular, the large altitude gap between LEO satellites and the ground implies long propagation distances and substantial delays.

To elaborate, we consider a bistatic localization system to reduce the reliance on ultra-fine angular resolution. Specifically, we propose a joint TN-NTN bistatic downlink architecture, where the LEO satellite serves as the transmitter providing wide coverage, while a terrestrial base station (BS) acts as the receiver and performs low-latency signal processing and localization. By jointly exploiting the time-frequency observations and the associated bistatic geometric constraints, the proposed framework enables robust high-accuracy localization both for moderate array sizes and under practical hardware requirements. In particular, the LEO satellite transmits downlink pilots and each vehicular user equipment (UE) is modelled as a non-cooperative scatterer characterized by its radar cross section (RCS), generating a bistatic return received at the BS.

By stacking the observations across the time-frequency pilot grids, the BS formulates a sparse joint time-frequency-spatial multiple measurement vector (MMV) model for channel-parameter recovery under hybrid beamforming. In contrast to classical MMV formulations that assume a common sensing matrix, the sensing matrix in our setup is symbol-dependent due to harnessing symbol-specific precoders/combiners. We therefore develop a modified block orthogonal matching pursuit (BOMP) that coherently aggregates correlations across time-frequency snapshots under time-varying sensing matrices. Building upon the recovered angular information, we then estimate the target-specific residual delay and Doppler via a two-dimensional (2D) matched filter, and finally obtain the UE position by combining the estimated angle and residual time of arrival (ToA) with an elliptic bistatic range constraint. Our contributions are boldly contrasted to the state-of-the-art in Table 2, and details are listed as follows:

- *System model:* We propose a unified LEO-UE-BS bistatic downlink localization framework in which the LEO satellite transmits pilots and the terrestrial BS performs localization, without relying on the ultra-fine angular resolution by leveraging time-frequency diversity, while satisfying the associated bistatic geometric constraints.
- *Algorithmic approach:* We formulate a sparse joint time-frequency-spatial MMV channel parameter estimation problem under hybrid beamforming, where the sensing matrix is symbol-dependent. To address this, we develop a modified BOMP that coherently aggregates correlations across time-frequency snapshots under time-varying sensing matrices and mitigates the impact of highly correlated dictionaries.
- *Localization phase:* We exploit the known LEO-BS geometry to perform timing advance and Doppler pre-compensation, so that the residual ToA and Doppler become target-specific. We then apply 2D matched filtering for estimating the residual delay-Doppler pair and combine it with the angle estimate via an explicit elliptic bistatic range constraint to infer the UE position.

TABLE 1. List of Main Variables

Symbol	Description	Symbol	Description
c	Speed of light	f_c	Carrier frequency
λ	Wavelength, $\lambda = c/f_c$	f_s	Subcarrier spacing
N_{sc}	Number of OFDM subcarriers	T	OFDM symbol duration, $T = 1/f_s$
M_s	Number of pilot OFDM symbols	P	Number of time-frequency snapshots, $P = M_s N_{sc}$
N_t	Number of LEO transmit antennas	N_t^x, N_t^y	LEO transmit UPA size along x/y axes
N_r	Number of BS receive antennas	N_r^x, N_r^y	BS receive UPA size along x/y axes
N_{rf}	Number of RF chains	K	Number of UEs
L_p	Number of propagation paths	$\mathbf{p}_{LEO}$	Position of LEO
$\mathbf{p}_{BS}$	Position of BS	$\mathbf{p}_k$	Position of k-th UE
$\theta_{k,l}^x, \theta_{k,l}^y$	Path angles on the x/y axes	$\mathbf{v}_t$	LEO transmit array response
$\mathbf{v}_r$	BS receive array response	τ_l	Delay of l-th path
v_l	Doppler shift of l-path	τ_l^{res}	Residual delay after timing advance (TA)
v_l^{res}	Residual Doppler after Doppler pre-compensation (DPC)	$g_{k,l}$	Complex path gain
$\mathcal{P}_{\text{PL}}$	Path-loss power gain	$\mathcal{P}_{\text{abs}}$	Atmospheric absorption transmittance
$\mathcal{P}_{\text{ref}}$	Reflection loss coefficient for NLoS paths	$\mathbf{H}_{k,m,n}$	MIMO channel for k-th UE at symbol m, subcarrier n
$\mathbf{F}_m$	LEO transmit precoder at m-th symbol	$\mathbf{W}_m$	BS receive combiner at m-th symbol
$\mathbf{s}_{k,m,n}$	Pilot vector of k-th UE on (m,n)-th snapshot	$\mathbf{y}_{m,n}$	Received BS signal on (m,n)-th snapshot
$\mathbf{z}_{m,n}$	AWGN vector	$\boldsymbol{\phi}_{m,i}$	Sensing row for RF chain i at symbol m
$\boldsymbol{\Phi}_m$	Stacked sensing matrix	$\mathbf{A}_t, \mathbf{A}_r$	Transmit/receive angular dictionaries
$\boldsymbol{\Gamma}$	Kronecker angular dictionary, $\boldsymbol{\Gamma} = \mathbf{A}_r \otimes \mathbf{A}_t$	$\boldsymbol{\Psi}_m$	Snapshot-based sensing matrix at m-th symbol
$\mathbf{h}_{m,n}$	Sparse angular-domain channel vector	$\mathcal{S}$	Joint sparse support across P snapshots
$S(g)$	MMV score for atom g in modified BOMP	$\mathbf{S}$	Time-frequency coefficient matrix for a selected atom
$\mathbf{a}_t(v)$	Temporal steering vector on Doppler grid	$\mathbf{a}_f(\tau)$	Frequency steering vector on delay grid
$C(v,\tau)$	2D matched-filter response	$\hat{v}^{\text{res}}, \hat{\tau}^{\text{res}}$	Estimated residual Doppler and delay
$\hat{\boldsymbol{\mu}}_r$	Estimated BS-side direction vector	$\mathbf{p}(s)$	BS-centered ray, $\mathbf{p}(s) = \mathbf{p}_{\text{BS}} + s\hat{\boldsymbol{\mu}}_r$
D	Total bistatic range, $D = \|\mathbf{p}_{\text{LEO}} - \mathbf{p}_{\text{BS}}\| + c\hat{\tau}^{\text{res}}$		

TABLE 2. Contrasting Our Novelty to the Literature

	[16]	[17]	[18]	[19]	[20]	[5]	[21]	[22]	[34]	[35]	**This work**
System Model											
DL NTN CE based localization				✓		✓		✓			✓
Single-satellite	✓			✓		✓					✓
LEO Bistatic sensing									✓	✓	✓
Algorithmic Approach											
Geometry-based precompensation		✓	✓								✓
Residual ToA & Doppler estimation							✓				✓
Joint time-frequency-spatial MMV											✓
Localization Phase											
Elliptic Constraints											✓

- *Validation:* Numerical results validate the proposed framework under realistic LEO-BS bistatic settings, demonstrating meter-level localization accuracy and illustrating the impact of pilot symbols/subcarriers allocation and angular resolution on localization robustness.

To the best of our knowledge, such a bistatic LEO based localization system using an MMV model and elliptic constraints has not been studied in the open literature. A list of main variables is included in Table 1. This paper is organized as follows: Section II introduces the system model. Our time-frequency-spatial MMV formulation is derived in Section III. Moreover, the system parameter setting and simulation results are investigated in Section IV. Finally, our conclusions are provided in Section V.

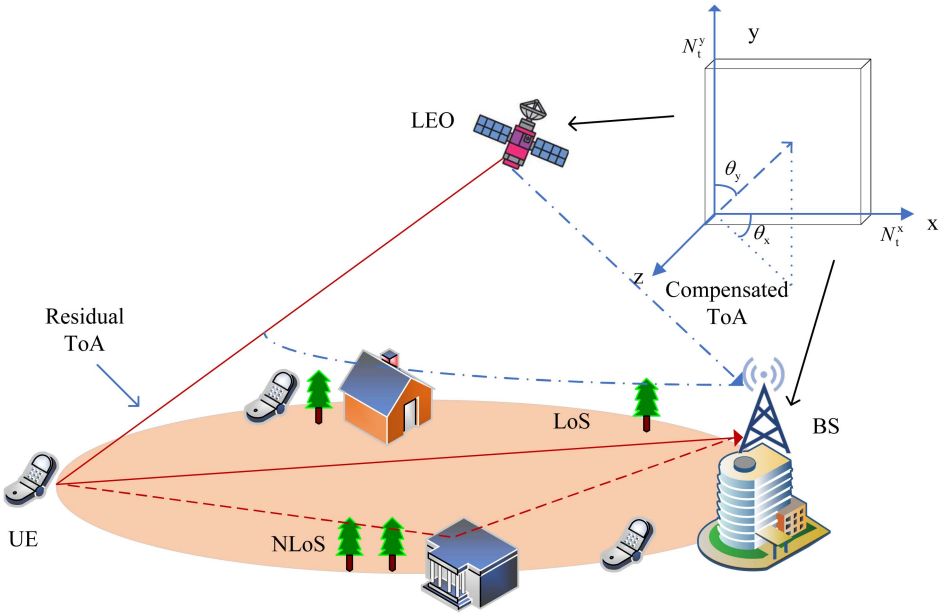

FIGURE 1. Geometry of downlink bistatic MIMO LEO based localization, where the locations of LEO and BS are known and UE is about to estimate.

Notations: a, $\mathbf{a}$, $\mathbf{A}$ stand for scalar, vector and matrix, respectively. $\mathbf{A}^{\mathrm{T}}$, $\mathbf{A}^{\mathrm{H}}$, $\mathbf{A}^{\dagger}$, $\|\mathbf{a}\|_2$ and $\|\mathbf{A}\|_F$ denote the transpose, Hermitian transpose, pseudoinverse, the Euclidean norm of vector $\mathbf{a}$, and the Frobenius norm of matrix $\mathbf{A}$, respectively. The (i, j)-th entry of $\mathbf{A}$ is $[\mathbf{A}]_{i,j}$, and diag($\mathbf{a}$) is a diagonal matrix formed by the diagonal elements of $\mathbf{a}$. $\mathbb{E}(\mathbf{A})$ is the expectation of $\mathbf{A}$, vec($\mathbf{A}$) is the vectorization operation of $\mathbf{A}$, mod(i, j) denotes the modulo operation, and $j = \sqrt{-1}$; $(\mathbf{A})^*$ represents the conjugate of matrix $\mathbf{A}$.

II. SYSTEM MODEL

Our space-air-ground-integrated networks (SAGIN) include a MIMO LEO satellite, a ground BS and K vehicular UE. We consider a downlink (DL) OFDM based LEO-UE-BS bistatic localization scenario relying on hybrid transmit precoding (TPC) and receive combining (RC) at the LEO transmitter and the BS receiver, respectively, where the vehicular UEs are the targets. The LEO and BS adopt uniform planar arrays (UPAs) of sizes $N_t = N_t^x N_t^y$ and $N_r = N_r^x N_r^y$, respectively, both lying on the xy-plane and pointing to the $+z$ half-space. Specifically, we assume that the subcarrier spacing is f_s and N_{sc} subcarriers are employed. The symbol duration is $T = 1/f_s$, while a pilot frame contains M_s OFDM pilot symbols, yielding $P = M_s N_{sc}$ snapshots per frame.

As illustrated in Fig. 1, the position and velocity of the LEO is inferred by the ground BS using the satellite calendar, denoted as $\mathbf{p}_{LEO} = [p_{LEO}^x, p_{LEO}^y, p_{LEO}^z]^T$ and $\dot{\mathbf{p}}_{LEO} = [\dot{p}_{LEO}^x, \dot{p}_{LEO}^y, \dot{p}_{LEO}^z]^T$, respectively. The ground BS is located at $\mathbf{p}_{BS} = [p_{BS}^x, p_{BS}^y, p_{BS}^z]^T$, and these are assumed to be known for delay and Doppler pre-compensation [37]. Additionally, we assume that all vehicular UEs are at unknown positions, formulated as $\mathbf{p}_k = [p_k^x, p_k^y, p_k^z]^T$ with $k = 1, \ldots, K$. Furthermore, we assume that the UEs are non-cooperative targets, where the reflection characteristic is quantified by its RCS [38].

A. CHANNEL MODEL

We define the transmit UPA response for the l-th propagation path of the k-th UE, formulated as [19]

$$\mathbf{v}_{k,l}^x = \frac{1}{\sqrt{N_t^x}} \Big[1, \exp\{-j\pi \sin\theta_{k,l}^y \cos\theta_{k,l}^x\}, \ldots, \times \exp\{-j\pi (N_t^x - 1) \sin\theta_{k,l}^y \cos\theta_{k,l}^x\}\Big]^T, \quad (1)$$

$$\mathbf{v}_{k,l}^y = \frac{1}{\sqrt{N_t^y}} \Big[1, \exp\{-j\pi \cos\theta_{k,l}^y\}, \ldots, \times \exp\left\{-j\pi (N_t^y - 1) \cos\theta_{k,l}^y\right\}\Big]^T, \quad (2)$$

where $\theta_{k,l}^x$ and $\theta_{k,l}^y$ denote the angles on the x and y axis, respectively. Since the LEO is typically deployed at an altitude significantly higher than the surrounding scatterers near the users, the angle of departure (AoD) $\boldsymbol{\theta}_{k,l}^t$ of the propagation paths associated with the k-th UE can be considered nearly identical, mathematically represented as $\boldsymbol{\theta}_{k,l}^t \triangleq \boldsymbol{\theta}_k^t$, $\forall l$. We drop the subscript l, and express the UPA response as $\mathbf{v}_{k,l}^t(f) = \mathbf{v}_k^t(f)$. Hence, we define $\mathbf{v}_{k,n}^t \triangleq \mathbf{v}_k^t(f_n)$. However, for the ground link between the BS and UEs, the non-line-of-sight (NLoS) path cannot be ignored. Under the assumption of perfect time and frequency synchronization[1], the effective channel matrix $\mathbf{H}_{k,m,n} \in \mathbb{C}^{N_r \times N_t}$ for the k-th UE over the nth

[1]The time frequency synchronization problem has been investigated in [39], which is outside the scope of this work.

subcarrier of the m-th OFDM symbol is formulated as follows:

$$\mathbf{H}_{k,m,n} = \sum_{l=0}^{L_p-1} g_{k,l}\, e^{j2\pi\left(v_{l,k}\, t_m - \tau_{l,k}\, f_n\right)}\, \mathbf{v}_r(\boldsymbol{\mu}_{r,l,k})\, \mathbf{v}_t(\boldsymbol{\mu}_{t,k})^H, \tag{3}$$

where $\tau_{l,k}$ and $v_{l,k}$ are the propagation delay and Doppler of l-th path, while $\boldsymbol{\mu}_{t,k}$ and $\boldsymbol{\mu}_{r,l,k}$ denote the transmit and receive spatial frequencies, respectively. The complex gain is denoted as $g_{k,l}$, and based on [10], it is modelled by a shadowed Rician fading distribution. The time-varying channel coefficient can be expressed as

$$g(t) = \underbrace{A(t)\exp\left[j\zeta(t)\right]}_{NLoS} + \underbrace{Z(t)\exp(j\xi)}_{LoS}, \tag{4}$$

where $A(t)$ follows the Rayleigh distribution with uniformly distributed phase $\zeta(t)$ and $Z(t)$ obeys the Nakagami-m distribution with a constant line-of-sight (LoS) phase ξ. Given that the average power levels of the NLoS and LoS components are $|A(t)|^2 = 2b_0$ and $|Z(t)|^2 = \Omega$, they satisfy the normalization $\Omega + 2b_0 = 1$ [10].

- *Path Loss*: The path loss gain is formulated as:

$$\mathcal{P}_{PL} = \left(\frac{c}{4\pi f_c}\right)^2 d^{-\alpha_p}, \tag{5}$$

  where c is the speed of light, f_c is the carrier frequency and α_p is the path loss exponent.
- *Atmospheric Absorption*: Given the optical thickness η_i, a Beer-Lambert-law-based model for the transmittance is expressed as [10]:

$$\mathcal{P}_{abs}(\eta_i) = \exp\left(-\sum\nolimits_i \eta_i\right). \tag{6}$$

  Note that the value of η_i for different frequency and gases can be found in [40].

Therefore, the complex gain for the target LoS link is formulated as $g_{k,0} = \sqrt{\Omega \mathcal{P}_{PL}\mathcal{P}_{abs}\mathcal{P}_{RCS}}$, where $\mathcal{P}_{RCS}$ represents the reflection power loss determined by the UE's RCS, denoted as $\sigma_{RCS,k}$. In addition, the power gain of the NLoS component is expressed as $g_{k,l} = \sqrt{2b_0 \mathcal{P}'_{PL}\mathcal{P}_{abs}\mathcal{P}_{RCS}\mathcal{P}_{ref}}$, where $\mathcal{P}'_{PL}$ denotes the path loss for the NLoS paths and $\mathcal{P}_{ref}$ represents the additional reflection loss caused by environmental scatterers.

B. SIGNAL MODEL

For the m-th pilot symbol and n-th subcarrier, the LEO applies a symbol-dependent TPC $\mathbf{F}_m \in \mathbb{C}^{N_t \times N_{rf}}$ and the BS applies a RC $\mathbf{W}_m \in \mathbb{C}^{N_r \times N_{rf}}$, where N_{rf} is the number of radio frequency (RF) chains. For each UE $k = 1, \ldots, K$, the LEO transmits a unit-power pilot $\mathbf{s}_{k,m,n} \in \mathbb{C}^{N_{rf} \times 1}$ on the snapshot (m, n).

The multiuser observation at the BS is expressed as

$$\mathbf{y}_{m,n} = \sum_{k=1}^{K} \mathbf{W}_m^H\, \mathbf{H}_{k,m,n}\, \mathbf{F}_m\, \mathbf{s}_{k,m,n} + \mathbf{z}_{m,n}, \tag{7}$$

where $\mathbf{z}_{m,n} \sim \mathcal{CN}(0, \sigma^2 \mathbf{I}_{N_{rf}})$ is the additive white Gaussian noise (AWGN).

To separate the k-th UE's signal, we assign pilots across the time-frequency set, where we enforce strict pilot orthogonality across users over the time–frequency pilot grids $\sum_{m=0}^{M_s-1}\sum_{n=0}^{N_{\mathrm{sc}}-1}(\mathbf{s}_{k,m,n})^H \mathbf{s}_{\widehat{k},m,n} = 0,\ \forall\, k \neq \widehat{k}$. Equivalently, over a selected pilot subset $\mathcal{G} = \{(m_p, n_p)\}_{p=1}^{M_s N_{sc}}$ associated with $|\mathcal{G}| = M_s N_{\mathrm{sc}}$, we have the k-th UE's receive signal after either Walsh-Hadamard or Zadoff-Chu sequences are spread across $\mathcal{G}$. Note that, the pilot non-orthogonality leads to multi-user interference, which has been extensively studied in the literature together with mitigation techniques, such as pilot decontamination and superimposed pilots [41], [42]. The related non-orthogonal signature based multi-user detection has also been widely investigated in compressive sensing based frameworks [43], [44]. In this paper, we focus our attention on the strictly-orthogonal pilot allocation case to characterize the proposed bistatic localization framework. Consequently, when focusing on a single UE, we drop the UE index k and use $\sigma_{RCS,k}$, $\mathbf{H}_{m,n}$ as well as $\mathbf{y}_{m,n}$ without ambiguity.

C. PRE-COMPENSATED RECEIVED SIGNAL MODEL

Conventional delay and Doppler estimation techniques in terrestrial OFDM systems often rely on FFT/IFFT-based signal processing methods [45]. These approaches are effective under moderate mobility and short propagation delay conditions. Therefore, timing advance (TA) and Doppler pre-compensation (DPC) is required in the non-terrestrial network [37], [46]. As the distance between the BS and UE is significantly lower than that between the LEO and UE, we exploit the location of the BS in support of the TA and DPC. Thus, the receive signal can be further expressed as

$$\widehat{\mathbf{y}}_{m,n} = \underbrace{\mathbf{W}_m^H\, \widehat{\mathbf{H}}_{m,n}\, \mathbf{F}_m \mathbf{s}_{m,n}}_{\tilde{\mathbf{y}}_{m,n}} + \mathbf{z}_{m,n}, \tag{8}$$

where $\widehat{\mathbf{H}}_{m,n} = \sum_{l=0}^{L_p-1} \alpha_l e^{j2\pi(v_l^{res} m T - \tau_l^{res} f_n)} \mathbf{v}^r(\mu_{r,l})\mathbf{v}^t(\mu_t)^H$, and v_l^{res}, τ_l^{res} denote the residual Doppler shift and delay for the l-th path, respectively.

Furthermore, Fig. 1 illustrates the considered DL LEO-UE-BS bistatic geometry and the geometry-aided pre-compensation concept, while Fig. 2 summarizes the corresponding signal processing flow. Specifically, as depicted in Fig. 1, by exploiting the known locations of the LEO and BS, TA and DPC are performed with respect to the LEO-BS reference, resulting in the pre-compensated receive signal model in (8). This is the first step shown in Fig. 2, converting the original propagation delay/Doppler into the residual quantities τ_l^{res} and v_l^{res}, which will be estimated.

III. PROBLEM FORMULATION

A. TIME-FREQUENCY-SPATIAL SPARSITY

We assume having a single pilot frame with M_s OFDM pilot symbols and N_{sc} subcarriers, yielding $M_s N_{\mathrm{sc}}$ snapshots. After DPC and TA with respect to the LEO-BS reference, each

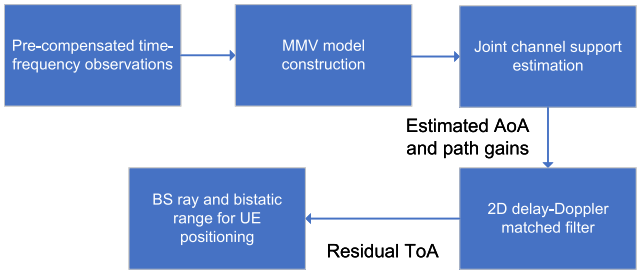

FIGURE 2. Flowchart of the proposed localization scheme using MMV model.

propagation path is characterized by a residual delay τ_l^{res} and residual Doppler v_l^{res}. For the m-th pilot symbol and the n-th subcarrier, the N_{rf}-dimensional receive signal vector at the BS is modelled as

$$\widehat{\mathbf{y}}_{m,n} = \sum_{l=0}^{L_p-1} \alpha_l \, e^{j2\pi\left(v_l^{\text{res}} t_m - \tau_l^{\text{res}} f_n\right)} \left(\mathbf{W}_m^H \mathbf{B}_l \, \mathbf{F}_m \mathbf{s}_{m,n}\right) + \mathbf{z}_{m,n}, \tag{9}$$

where we have $t_m = (m-1)T$, $f_n = (n - \frac{N_{\text{sc}}-1}{2})f_s$, $\mathbf{B}_l = \mathbf{v}^r(\boldsymbol{\mu}_{r,l})\,\mathbf{v}^t(\mu_t)^H$, while $\mathbf{F}_m \in \mathbb{C}^{N_t \times N_{rf}}$, and $\mathbf{W}_m \in \mathbb{C}^{N_r \times N_{rf}}$ are the per-symbol hybrid beams with unit-norm columns.

Let us define the sensing row for the i-th RF chain at time m, and assume identical pilot symbols across all subcarriers, i.e $\mathbf{s}_{m,n} = \mathbf{s}_m$. Then, we have

$$\boldsymbol{\phi}_{m,i} = \left(s_{m,i}\mathbf{f}_{m,i}^T \otimes \mathbf{w}_{m,i}^H\right) \in \mathbb{C}^{1\times(N_t N_r)}, \tag{10}$$

with $\mathbf{f}_{m,i}$ and $\mathbf{w}_{m,i}$ being the i-th columns of $\mathbf{F}_m$ and $\mathbf{W}_m$, respectively. Stacking the $\boldsymbol{\phi}_{m,i}$ values for $i = 1, \ldots, N_{rf}$ yields

$$\boldsymbol{\Phi}_m = \begin{bmatrix} s_{m,1}\mathbf{f}_{m,1}^T \otimes \mathbf{w}_{m,1}^H \\ \vdots \\ s_{m,N_{rf}}\mathbf{f}_{m,N_{\text{rf}}}^T \otimes \mathbf{w}_{m,N_{\text{rf}}}^H \end{bmatrix} \in \mathbb{C}^{N_{\text{rf}}\times(N_t N_r)}. \tag{11}$$

Then, the UPA's angular dictionaries are given by

$$\begin{aligned} \mathbf{A}_t &= \left[\mathbf{a}_t(\tilde{\boldsymbol{\mu}}_{t,1}), \ldots, \mathbf{a}_t(\tilde{\boldsymbol{\mu}}_{t,G_t})\right], \\ \mathbf{A}_r &= \left[\mathbf{a}_r(\tilde{\boldsymbol{\mu}}_{r,1}), \ldots, \mathbf{a}_r(\tilde{\boldsymbol{\mu}}_{r,G_r})\right]. \end{aligned} \tag{12}$$

where $\tilde{\boldsymbol{\mu}}_{t,j}$ and $\tilde{\boldsymbol{\mu}}_{r,j}$, $j = 1, \ldots, G_t/G_r$ denote the predefined 2D spatial-frequency grids at the LEO and the BS, respectively. Since each candidate path is characterized by one point of the receive grid and the transmit grid, the corresponding joint transmit receive atom becomes separable in the vectorized domain. Therefore, the overall angular dictionary of the vectorized channel is constructed as

$$\boldsymbol{\Gamma} \triangleq \mathbf{A}_r \otimes \mathbf{A}_t \in \mathbb{C}^{(N_t N_r)\times(G_r G_t)}. \tag{13}$$

Therefore, the snapshot-based sensing matrix is represented as

$$\boldsymbol{\Psi}_m \triangleq \left[\boldsymbol{\phi}_{m,1}\boldsymbol{\Gamma}; \ldots; \boldsymbol{\phi}_{m,N_{rf}}\boldsymbol{\Gamma}\right] \in \mathbb{C}^{N_{rf}\times(G_r G_t)}, \tag{14}$$

followed by per-column ℓ_2-normalization for stabilizing the MMV pursuit. Therefore, the stacked MMV signal at the RF receive combiner may be expressed as follows:

$$\hat{\mathbf{y}}_{m,n} = \boldsymbol{\Psi}_m \mathbf{h}_{m,n} + \mathbf{z}_{m,n}, \tag{15}$$

where $\hat{\mathbf{y}}_{m,n} \in \mathbb{C}^{N_{rf}\times 1}$ represents the stacked RF chain observations and $\mathbf{h}_{m,n}$ is a $G_r G_t \times 1$ angular-domain channel vector at the (m,n)-th snapshot, whose sparse support remains unchanged during the (m,n)-th time-frequency resources after TA and DPC.

In summary, assuming identical pilots across subcarriers, the rows of the sensing matrix are defined in (10) and stacked into $\boldsymbol{\Phi}_m$ in (11). With the UPA angular dictionaries in (12) and the Kronecker dictionary $\boldsymbol{\Gamma}$ in (13), we form the snapshot-based sensing matrix $\boldsymbol{\Psi}_m$ in (14), leading to the sparse linear model in (15). The MMV construction is illustrated as the second stage in Fig. 2.

B. MODIFIED BOMP ASSISTED LOCATION INFORMATION RECOVERY

Recall from (15) that each snapshot satisfies

$$\mathbf{y}_p \;=\; \boldsymbol{\Psi}_{m(p)}\,\mathbf{h}_p \;+\; \mathbf{z}_p, \qquad p = 1, \ldots, P, \tag{16}$$

where we have $P = M_s N_{\text{sc}}$ snapshots indexed by p, and $\Psi_{m(p)}$ denotes the sensing matrix corresponding to the pilot symbol index $m(p)$. Owing to the in common propagation paths, all angular-domain channel vectors share the joint sparse support of:

$$\mathcal{S} = \text{supp}(\mathbf{h}_1) = \cdots = \text{supp}(\mathbf{h}_P) \subset \{1, \ldots, G_r G_t\}, \tag{17}$$

where supp denotes the sparse support. Before the MMV pursuit, we normalize each $\boldsymbol{\Psi}_m$ on a column by column basis to unit ℓ_2-norm to stabilize the atom selection across heterogeneous sensing matrices. A modified BOMP is then harnessed for selecting L_p atoms by maximizing the sum of per-snapshot correlations over all P noisy measurements.

1) Initialization: Set $\mathcal{S} \leftarrow \emptyset$, and initialize the residuals as $\mathbf{r}_p \leftarrow \mathbf{y}_p$ for all $p = 1, \ldots, P$.

2) Atom selection at iteration $t = 0, \ldots, L_p - 1$: Let $\boldsymbol{\omega}_{p,g} \triangleq \Psi_{m(p)}(:, g)$ be the g-th column of $\Psi_{m(p)}$, which corresponds to the g-th transmit-receive angular atom. We then quantify the MMV score of

$$S(g) \;=\; \sum_{p=1}^{P} \left|\boldsymbol{\omega}_{p,g}^H \mathbf{r}_p\right|^2, \tag{18}$$

and select $\widehat{g} = \arg\max_g S(g)$. The joint support is updated as $\mathcal{S} \leftarrow \mathcal{S} \cup \{\widehat{g}\}$.

3) Least-squares (LS) update (per snapshot): For each p, we form the reduced sensing matrix $\mathbf{A}_p = \Psi_{m(p)}(:, \mathcal{S})$ and solve the per-snapshot least-squares problem of

$$\begin{aligned} \widehat{\mathbf{h}}_p \;&=\; \arg\min_{\mathbf{x}} \|\mathbf{y}_p - \mathbf{A}_p\mathbf{x}\|_2^2 \;=\; \mathbf{A}_p^{\dagger}\mathbf{y}_p, \\ \mathbf{r}_p &= \mathbf{y}_p - \mathbf{A}_p\,\widehat{\mathbf{h}}_p, \end{aligned} \tag{19}$$

Algorithm 1: Modified BOMP for Joint Angular Support Recovery Across P Snapshots.

Input: $\{\mathbf{y}_p\}_{p=1}^{M_s N_{\mathrm{sc}}}$, $\{\Psi_m\}_{m=1}^{M_s}$, L_p
Normalize: For each m, scale columns of $\mathbf{\Psi}_m$ to unit ℓ_2-norm
Initial: $\mathcal{S} \leftarrow \emptyset$; $\mathbf{r}_p \leftarrow \mathbf{y}_p$ for $p = 1, \ldots, M_s N_{\mathrm{sc}}$
for $t = 0, \ldots, L_p - 1$ **do**
    Score: For each $g \in \{1, \ldots, G_r G_t\}$,

$$S(g) \;=\; \sum_{p=1}^{M_s N_{\mathrm{sc}}} \left| \mathbf{\Psi}_{m(p)}(:, g)^H \, \mathbf{r}_p \right|^2$$

    Select: $\widehat{g} \leftarrow \arg\max_g S(g)$; $\mathcal{S} \leftarrow \mathcal{S} \cup \{\widehat{g}\}$
    LS update (per snapshot):
For each p, $\mathbf{A}_p = \Psi_{m(p)}(:, \mathcal{S})$, $\widehat{\mathbf{h}}_p \leftarrow \arg\min_{\mathbf{x}} \|\mathbf{y}_p - \mathbf{A}_p \mathbf{x}\|_2^2 = \mathbf{A}_p^{\dagger} \mathbf{y}_p$, $\mathbf{r}_p \leftarrow \mathbf{y}_p - \mathbf{A}_p \widehat{\mathbf{h}}_p$
end for
Output: Support $\widehat{\mathcal{S}} = \{g_1, \ldots, g_{L_p}\}$ and coefficients $\{\widehat{\mathbf{h}}_p\}_{p=1}^{M_s N_{\mathrm{sc}}}$

followed by residual update. Steps 2)-3) are then repeated until $|\mathcal{S}| = L_p$.

4) Outputs and mapping over the time–frequency grid: At convergence we obtain the joint support $\widehat{\mathcal{S}} = \{g_0, \ldots, g_{L_p - 1}\}$ and the angular-domain coefficients $\{\widehat{\mathbf{h}}_p\}_{p=1}^{P}$. Each index g_l uniquely maps to an AoA/AoD grid pair $(i_{r,l}, i_{t,l})$ in the receive and transmit angular dictionaries, thereby providing coarse angular estimates. For subsequent delay–Doppler processing, the coefficients associated with g_l are reshaped over the time–frequency plane into $\mathbf{S}^{(l)} \in \mathbb{C}^{M_s \times N_{\mathrm{sc}}}$, with

$$[\mathbf{S}^{(l)}]_{m,n} = \left[\widehat{\mathbf{h}}_{(m-1)N_{\mathrm{sc}}+n}\right]_{g_l}, \tag{20}$$

which is then used for estimating the residual Doppler and delay pair $(\hat{v}_l^{\mathrm{res}}, \hat{\tau}_l^{\mathrm{res}})$ via the 2D matched filter of Section III-C. The modified BOMP procedure is summarized in Algorithm 1.

Remark: The proposed procedure can be regarded as a generalized BOMP algorithm that is specifically tailored for the heterogeneous sensing matrices arising from beamforming. Compared to BOMP with its time-varying sensing matrix, defined as $\mathbf{\Psi}_m$, the classical simultaneous orthogonal matching pursuit (SOMP) has a time-invariant sensing matrix, denoted as $\mathbf{\Psi}$. By contrast, in our MMV model, each snapshot p is observed through a symbol-dependent sensing matrix $\mathbf{\Psi}_{m(p)}$ defined in (15), which reflects the varying TPCs/RCs over m. The MMV score in (18) therefore aggregates correlations across both the time- and frequency-domain, while appropriately accounting for per-symbol sensing. This joint processing exploits the fact that the physical paths remain unchanged within a pilot frame, so that even if some snapshots are heavily noise-contaminated owing to being poorly illuminated by a specific beam pattern, the corresponding atoms can still be reliably detected by pooling information from the remaining snapshots.

5) Spatial-frequency estimation and mapping to angles: Recall from (12), (13) and (14) that the angular dictionary is constructed as

$$\mathbf{\Gamma} \;=\; \mathbf{A}_r \otimes \mathbf{A}_t \in \mathbb{C}^{N_t N_r \times G_r G_t}, \tag{21}$$

where the transmit and receive dictionaries are defined as

$$\begin{aligned} \mathbf{A}_t &= \left[\mathbf{a}_t(\tilde{\boldsymbol{\mu}}_{t,1}), \ldots, \mathbf{a}_t(\tilde{\boldsymbol{\mu}}_{t,G_t})\right], \\ \mathbf{A}_r &= \left[\mathbf{a}_r(\tilde{\boldsymbol{\mu}}_{r,1}), \ldots, \mathbf{a}_r(\tilde{\boldsymbol{\mu}}_{r,G_r})\right], \end{aligned} \tag{22}$$

which sample the UPA steering vectors on a predefined 2D spatial-frequency grid $\{\tilde{\boldsymbol{\mu}}_{t,j}\}$ and $\{\tilde{\boldsymbol{\mu}}_{r,i}\}$. Hence, each column index $g \in \{1, \ldots, G_r G_t\}$ uniquely corresponds to a pair $[i_r(g), i_t(g)]$ and, in turn, to a transmit/receive spatial-frequency pair $(\tilde{\boldsymbol{\mu}}_{r,i_r(g)}, \tilde{\boldsymbol{\mu}}_{t,i_t(g)})$. Once the joint support $\widehat{\mathcal{S}}$ is recovered, the spatial-frequency estimates for the l-th path are obtained by searching the grid points as

$$\begin{aligned} \widehat{\boldsymbol{\mu}}_{r,l} &= \tilde{\boldsymbol{\mu}}_{r,\, i_r(g_l)}, \\ \widehat{\boldsymbol{\mu}}_{t,l} &= \tilde{\boldsymbol{\mu}}_{t,\, i_t(g_l)}. \end{aligned} \tag{23}$$

The spatial frequencies are related to the physical azimuth/elevation angles θ_x and θ_y, which can be evaluated as

$$\begin{aligned} \mu_x &= \sin\theta_y \cos\theta_x, \\ \mu_y &= \cos\theta_y, \end{aligned} \tag{24}$$

under half-wavelength inter-element spacing. Therefore, the BS-side AoA associated with the LoS atom $\widehat{g}$ can be reconstructed from the estimated spatial-frequency vector $\widehat{\boldsymbol{\mu}}_r$ by inverting these relationships as follows:

$$\begin{aligned} \widehat{\theta}_y &= \arccos\left(\widehat{\mu}_y\right), \\ \widehat{\theta}_x &= \operatorname{atan2}\left(-\widehat{\mu}_x, \sqrt{1 - \widehat{\mu}_y^2}\right), \end{aligned} \tag{25}$$

where $\widehat{\mu}_x$ and $\widehat{\mu}_y$ denote the components of $\widehat{\boldsymbol{\mu}}_r$. As shown in Fig. 2, in the third stage, the modified BOMP algorithm is employed for estimating the AoA and path gains based on the MMV model constructed in the previous subsection. More explicitly, across P snapshots, the modified BOMP algorithm exploits the joint sparsity assumption in (17) and selects the dominant angular atoms by maximizing the MMV score in (18), followed by the per-snapshot LS update in (19). The recovered coefficients are then mapped over the time–frequency grid as in (20). The resultant unit-norm spatial-frequency (or direction) vector $\widehat{\boldsymbol{\mu}}_r$ will then be used in Section III-C to form the BS-centered ray and, together with the bistatic range constraint, to recover the UE position.

C. RESIDUAL DELAY-DOPPLER ESTIMATION AND UE POSITION RECOVERY

Let $\widehat{g} \in \widehat{\mathcal{S}}$ denote the selected atom (e.g., the strongest LoS when $l = 0$), and then collect its coefficients across (m, n) into

$$\mathbf{S} \in \mathbb{C}^{M_s \times N_{\mathrm{sc}}}, \qquad [\mathbf{S}]_{m,n} \;=\; [\,\widehat{\mathbf{h}}_{(m-1)N_{\mathrm{sc}}+n}\,]_{\widehat{g}}. \tag{26}$$

Afterwards, the upsampling delay-Doppler grids in the temporal and frequency steering vectors are defined as $\mathcal{V} = \{v\}$ and $\mathcal{T} = \{\tau\}$ as $\mathbf{a}_t(v) = [e^{j2\pi t_m v}]_{m=1}^{M_s}$, $\mathbf{a}_f(\tau) = [e^{j2\pi f_n \tau}]_{n=1}^{N_{\text{sc}}}$. The 2D matched-filter response is

$$\mathbf{C}(v, \tau) \;=\; \big|\, \mathbf{a}_t(v)^H \, \mathbf{S} \, \mathbf{a}_f(\tau) \,\big|. \tag{27}$$

The residual estimates are obtained by the peak of $\mathbf{C}$ as

$$(\hat{v}^{\text{res}},\ \hat{\tau}^{\text{res}}) \;=\; \arg \max_{v\in\mathcal{V},\ \tau\in\mathcal{T}} \mathbf{C}(v, \tau). \tag{28}$$

The spatial frequencies at the BS associated with $\widehat{g}$ is $\hat{\boldsymbol{\mu}}_r = [\hat{\mu}_x, \hat{\mu}_y, \hat{\mu}_z]^T$ with $\hat{\mu}_z = -\sqrt{\max(0, 1 - \hat{\mu}_x^2 - \hat{\mu}_y^2)}$. The UE is assumed to lie along the ray $\mathbf{p}(s) \;=\; \mathbf{p}_{\text{BS}} + s\,\hat{\boldsymbol{\mu}}_r, s \geq 0$, as depicted in Fig. 1. Let D denote the bistatic range implied by the residual delay, represented as

$$D \;\triangleq\; \|\mathbf{p}_{LEO} - \mathbf{p}_{BS}\| \;+\; c\,\hat{\tau}^{res}. \tag{29}$$

The total distance satisfies the constraint

$$\zeta(s) \;\triangleq\; \big\|\mathbf{p}_{LEO} - \mathbf{p}(s)\big\| \;+\; s \;-\; D \;=\; 0. \tag{30}$$

We obtain a feasible $\widehat{s} \geq 0$ by a 1-D search formulated as

$$\widehat{s} \;=\; \arg \min_{s\in[0,\ 2D]} \zeta(s)^2, \tag{31}$$

and form the position candidate of the UE $\widehat{\mathbf{p}} = \mathbf{p}_{BS} + \widehat{s}\,\hat{\boldsymbol{u}}_r$.

As shown in the fourth stage of Fig. 2, the residual delay $\hat{\tau}^{\text{res}}$ and Doppler $\hat{v}^{\text{res}}$ are estimated by (28), and the final recovery of the UE's position is then estimated as the last stage.

In summary, Fig. 1 presents the DL LEO–UE–BS bistatic geometry and the TA/DPC intuition, while Fig. 2 translates this physical setup into the corresponding end-to-end signal processing used for channel/angle estimation and residual delay–Doppler aided localization. The pre-compensated time–frequency observations are first cast into a joint time–frequency–spatial MMV sparse model and processed by a modified BOMP algorithm to estimate the common angular support and path gains, after which a 2D delay–Doppler matched filter is applied to obtain the residual ToA/Doppler. The UE's position is finally recovered by intersecting the estimated BS beam with the bistatic range.

Remark: It is worth noting that the proposed CS-based framework possesses inherent robustness against multi-path clutter. Since the channel is modeled as a sparse combination of dictionary atoms, the separation of the target path from clutter is achieved through atomic decomposition in the joint time-frequency-spatial domain. Specifically, the greedy recovery algorithm identifies paths based on their correlation with the receive signal. In the scenario considered, the LEO-UE-BS link typically acts as the dominant component having the highest energy, attributed to the significant RCS of the vehicular target relative to the weaker diffuse scattering from environmental clutter. Therefore, the algorithm preferentially selects the atom corresponding to the target's AoA and delay in the initial iterations, effectively isolating the vehicular UE's location from NLoS multi-path interference.

TABLE 3. Computational Complexity Comparison of Different Algorithms

Algorithms	Computational complexity
Oracle-LS	$\mathcal{O}(M_s N_{sc} N_{rf})$
OMP-SMV	$\mathcal{O}(N_{rf} G_r G_t) + \mathcal{O}(M_s N_{sc} N_{rf})$
CoSaMP-SMV	$\mathcal{O}(2T_{\text{CoSaMP}} N_{rf} G_r G_t) + \mathcal{O}(M_s N_{sc} N_{rf})$
Proposed	$\mathcal{O}(M_s N_{sc} N_{rf} G_r G_t)$
LMMSE	$\mathcal{O}(2M_s N_{sc} T_{\text{LMMSE}} N_{rf} G_r G_t)$
AMP-MMV	$\mathcal{O}(2T_{AMP} M_s N_{sc} N_{rf} G_r G_t)$

IV. PERFORMANCE EVALUATION

Again, we consider the LEO-UE-BS bistatic downlink transmission shown in Fig. 1, where the positions of the LEO and BS are $\mathbf{p}_{LEO} = [100,\ 200,\ 300]^T$ km with the satellite's instant velocity of 7 km/s along the x-axis, and $\mathbf{p}_{BS} = [-50,\ 190,\ 100]^T$ m, respectively. The location of the UE is assumed to be the origin. The scatterers are randomly generated between the UE and BS. Moreover, the carrier frequency is set to $f_c = 28$ GHz, with subcarrier spacing of $f_s = 120$ kHz, $c = 3\times10^8$ m/s, and using half-wavelength element spacing. The number of antennas of the UPAs at the LEO and BS are $N_t = N_{t,x}N_{t,y} = 4 \times 4 = 16$, $N_r = N_{r,x}N_{r,y} = 4 \times 4 = 16$. Furthermore, $G_r = G_t = G \times G$, where G is the number of quantization levels for both $N_{t,x}$ and $N_{t,y}$ or $N_{r,x}$ and $N_{r,y}$. We assume a vehicular target with an RCS of $\sigma_{RCS} \approx 100\ \text{m}^2$ (20 dBsm), which is consistent with empirical measurements for multi-passenger vehicles at Ka-band [47][2]. The receive signal-to-noise ratio (SNR) is defined as $\mathbb{E}\left\{\|\tilde{\mathbf{y}}_{m,n}\|_2^2\right\} / \mathbb{E}\left\{\|\mathbf{z}_{m,n}\|_2^2\right\}$, averaged over P time-frequency snapshots within a pilot frame, which results in processing gain by stacking P snapshots via MMV support recovery and 2D matched filtering. The number of Monte Carlo trials is set to 1500.

The benchmarks considered in this paper include 1) oracle-least square (LS), 2) orthogonal matching pursuit (OMP) with single measurement vector (SMV) [49], 3) linear minimum mean square error (LMMSE), 4) compressed sampling matching pursuit (CoSaMP) [50] and 5) approximate message passing (AMP) [51], [52]. The complexity of these algorithms is summarized in Table 3, where T_{CoSaMP}, T_{AMP}, T_{LMMSE} denote the number of iterations for the different algorithms. Note that the LMMSE estimator relies on the conjugate gradient algorithm, which avoids explicit inversion of the $(G_rG_t \times G_rG_t)$-element covariance matrix, and each iteration only requires two matrix–vector multiplications with the sensing matrix and its Hermitian.

[2]To justify the physical feasibility of the bistatic link at 28 GHz, we assume a Ka-band LEO satellite having an EIRP of 43.1 dBW [48]. For instance, for a vehicular UE associated with an effective RCS of 20 dBsm located 300 km from the LEO and 50 m from the BS, the receive power is approximately −106 dBm with the receive antenna gain of 16 dBi. When considering a noise power of −108 dBm, the receive SNR is 1.5 dB.

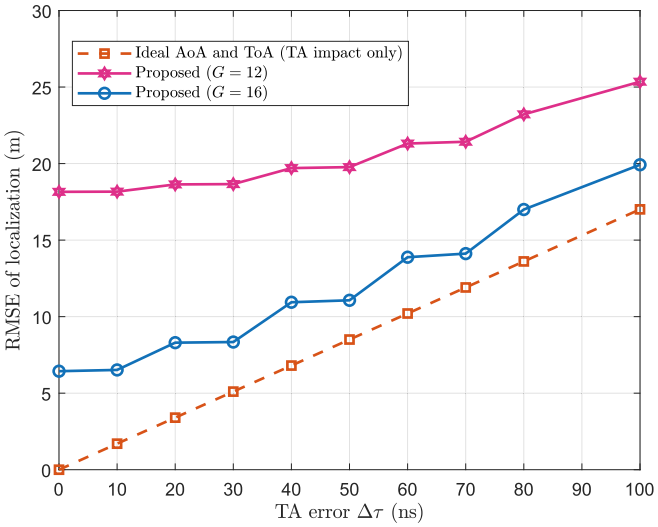

FIGURE 3. RMSE performance of localization accuracy versus different TA errors, when $M_s = 8$, $N_{sc} = 32$ and SNR=0 dB.

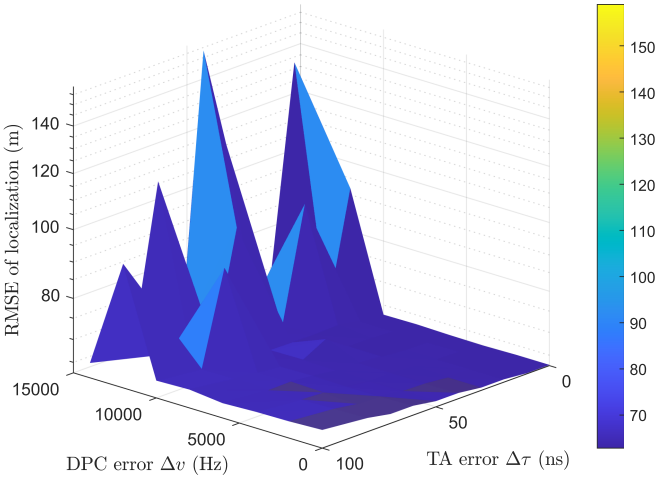

FIGURE 4. The RMSE performance of localization accuracy versus different TA and DPC errors, when we have $M_s = 32$, $N_{sc} = 32$ and SNR= 0 dB.

The estimation performance is characterized by the root mean squared error (RMSE), defined as:

$$\text{RMSE} = \sqrt{\frac{1}{k_{\text{monte}}} \sum_{k_{\text{monte}}=1}^{K_{\text{monte}}} \left\| \widehat{\mathbf{q}}_{k_{\text{monte}}} - \mathbf{q}_{k_{\text{monte}}} \right\|_2^2}, \tag{32}$$

where K denotes the number of Monte Carlo trials, and $\mathbf{q}$ and $\widehat{\mathbf{q}}$ are the true and estimated values, respectively.

Fig. 3 illustrates the impact of the TA error $\Delta\tau$ on the localization RMSE for different beamspace resolutions. It is worth noting that $\Delta\tau$ essentially reflects the potential errors in the prior LEO-BS geometry information and synchronization mismatches. The dashed curve represents the geometric lower bound obtained when the AoA/AoD and residual ToA are assumed to be perfectly estimated and only the TA mismatch is propagated through the bistatic ellipse. As expected, this RMSE trend evolves almost linearly with $\Delta\tau$, indicating that a small synchronization error in the LEO-BS reference link gradually aggravates the position bias. Furthermore, the proposed scheme follows this trend with a near-constant gap of only a few meters, which indicates that the main performance degradation is imposed by the TA misalignment, rather than by the compressed sensing estimation itself for a sufficiently fine beamspace grid. In particular, for $\Delta\tau \leq 40$ ns, the proposed scheme still achieves sub-10m RMSE, yielding a reasonable robustness to moderate TA errors. By contrast, when the angular grid is coarser ($G = 12$), the RMSE increased to about 18-25 m for $\Delta\tau < 100$ ns. This confirms that in the coarse-grid regime, the localization accuracy is mainly limited by the beamspace angular quantization error, and any further refinement of the TA/DPC yields marginal benefits.

Fig. 4 shows the localization sensitivity to TA residual error $\Delta\tau$ and DPC error Δv, when we set $M_s = 32$, $N_{sc} = 32$, and SNR $= 0$ dB. From the simulation results in Fig. 4, we conclude that after the TA pre-compensation, moderate residual TA errors mainly introduce a mild bias in the residual delay estimate and do not fundamentally break the angle-delay association. By contrast, the RMSE becomes highly sensitive to the DPC mismatch for $\Delta v > 5$ kHz. This behavior is consistent with a Doppler-mismatch effect, where the residual Doppler induces symbol-to-symbol phase rotation and the loss of coherent combining across the M_s pilot symbols, which shifts the matched filter response in the delay-Doppler domain. Therefore, a wrong bistatic range estimate is employed to recover the target's location, and thus causes a large positioning error, even though the final geometric solver only uses the residual delay. Therefore, the residual Doppler estimation is necessary for reliable delay extraction and corresponding localization.

To evaluate the trade-off between hardware complexity (number of RF chains, denoted as N_{rf}) and beamspace resolution G, Fig. 5 presents the localization RMSE versus SNR for various combinations of $N_{rf} \in \{8, 16\}$ and quantization levels $G \in \{8, 12, 16\}$. Observed in Fig. 5 that when the number of quantization levels G is increased, which means that the beamspace resolution increases, the estimation of the AoA and the residual delay becomes more accurate. Specifically, the localization accuracy can be improved from about 60 meters to about 6 meters by increasing G from 8 to 16. Furthermore, when N_{rf} is increased from 8 to 16, there is a further 4 dB gain at SNR$=-6$ dB, concluding that higher hardware complexity results in better beamforming gain and MMV recovery even under the same angular resolution.

Next, we investigate the impact of pilot overhead in Fig. 6. The specific grid of M_s and N_{sc} values are chosen to illustrate the effect of the joint time-frequency diversity gain on the estimation accuracy. Explicitly, Fig. 6 highlights the benefit of increasing the time–frequency pilot overhead. Increasing M_s improves Doppler estimation, while increasing N_{sc} improves the delay estimation. Their combined benefit reduces the positioning error roughly in line with the product of $M_s N_{sc}$.

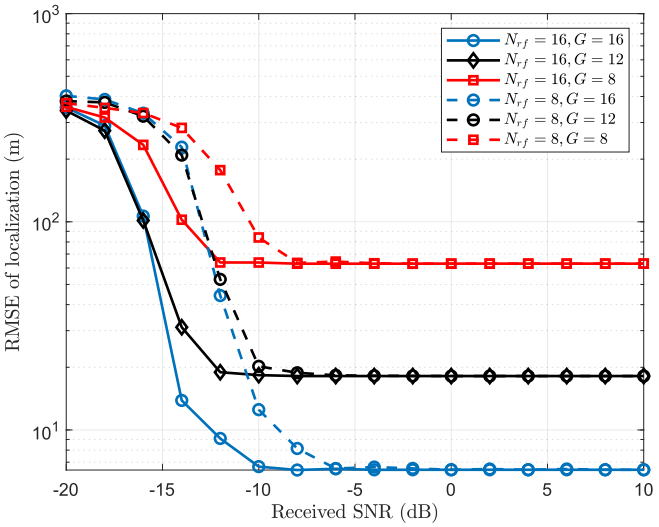

FIGURE 5. The RMSE performance of localization accuracy with different angular quantization levels, when $M_s = 8$ and $N_{sc} = 32$.

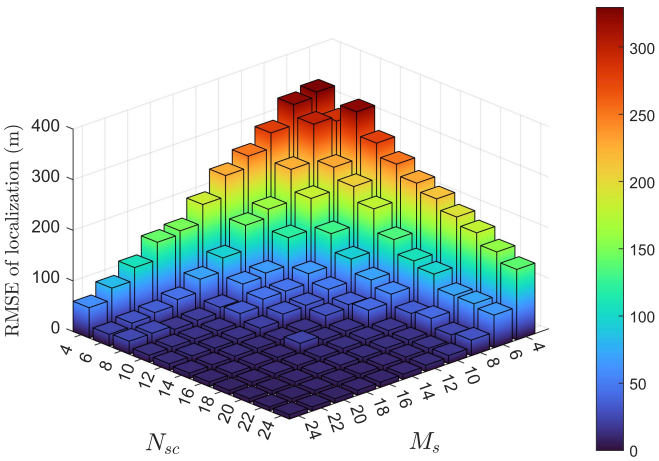

FIGURE 6. The RMSE performance of localization accuracy with different M_s and N_{sc}, when $N_{rf} = 4$, $G = 16$ and SNR $= -6$ dB.

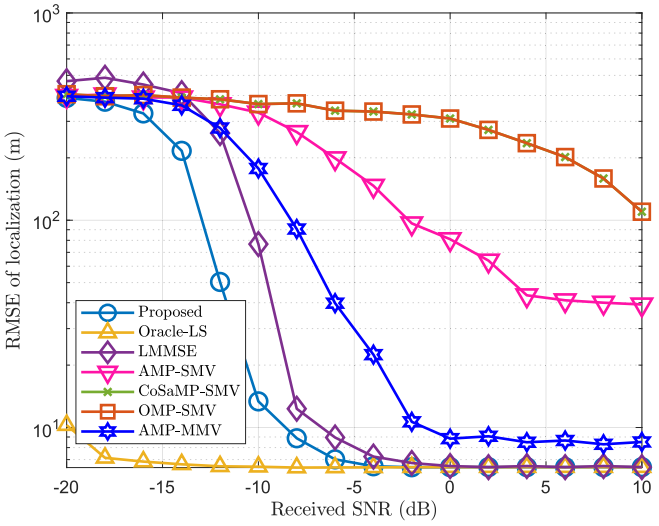

FIGURE 7. The RMSE performance of localization accuracy with different compressed sensing algorithms, when we set $M_s = 8$, $N_{sc} = 32$, $N_{rf} = 8$, and $G = 16$.

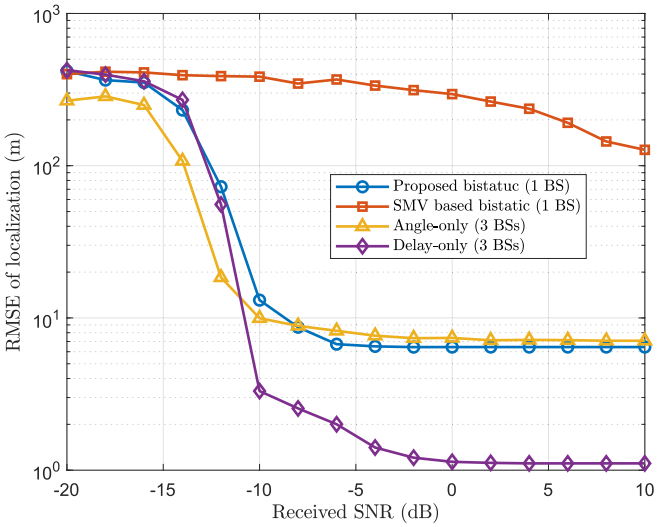

FIGURE 8. The RMSE performance of localization accuracy versus different localization baselines.

Furthermore, the channel estimation performance also improves with more snapshots. Moreover, it can be observed that the localization accuracy is more sensitive to M_s, which is because a higher M_s improves training diversity in (15), leading to better MMV conditions.

Fig. 7 compares the localization accuracy against the state-of-the-art channel estimation algorithms. To ensure a fair comparison, we fix the system parameters to a representative operating point ($M_s = 8, N_{sc} = 32, N_{rf} = 8, G = 16$), which balances resource consumption and potential accuracy. The Oracle-LS curve provides an upper performance bound, since it assumes perfect knowledge of the true support and only estimates the path coefficients. Hence its high-SNR behavior is almost flat and it is mainly limited by the AoA/AoD and delay/Doppler grid quantization. The proposed joint MMV scheme exhibits a threshold around SNR$=-6$ dB and then rapidly converges to the Oracle-LS floor, confirming that fully exploiting the joint sparsity across all time–frequency snapshots is highly beneficial for localization. The LMMSE exhibits a estimator residual RMSE. However, as seen in Fig. 7, the global shrinkage of its coefficients leads to less reliable support selection at low SNR than the proposed solution. In AMP-SMV, the AMP algorithm is run independently for each OFDM symbol, so the snapshots are processed separately and no joint inter-symbol sparsity is exploited. Its performance improves only gradually with the SNR and remains clearly inferior to the proposed scheme. By contrast, AMP-MMV jointly processes all OFDM symbols under a common-support based MMV model, which yields a noticeable SNR gain and allows it to approach the oracle floor. However, a small gap persists because AMP is sensitive to

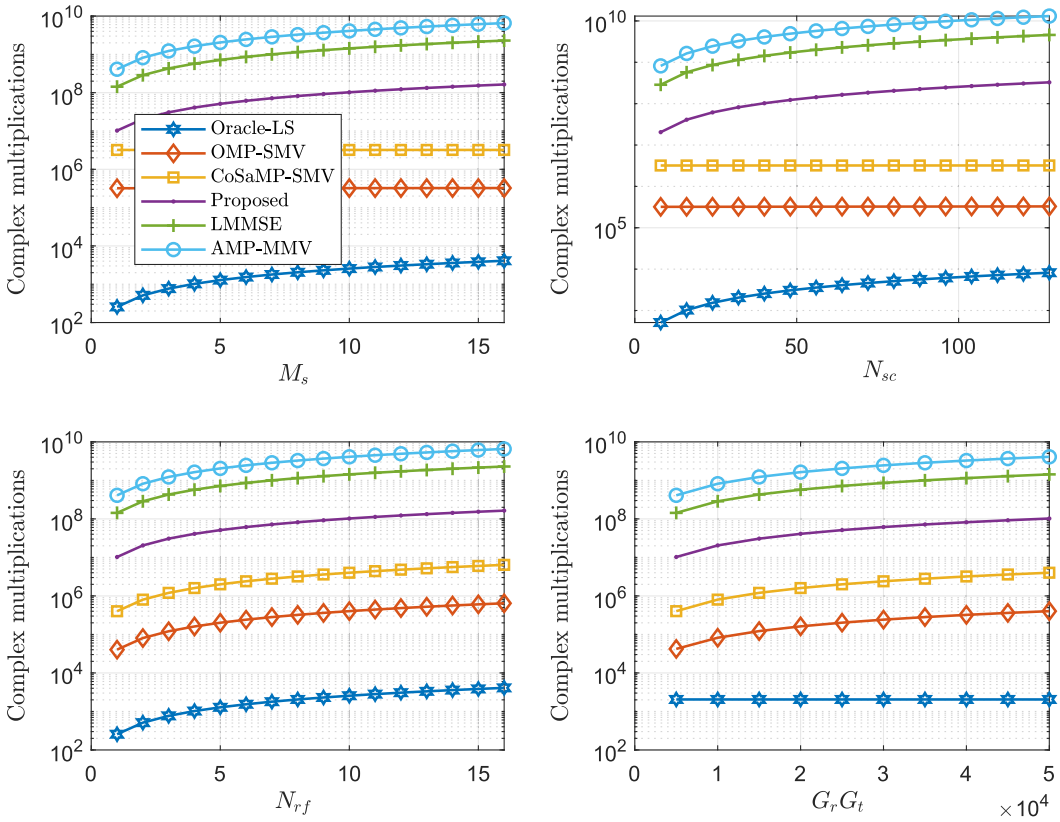

FIGURE 9. The comparison of different algorithms, including Oracle-LS, OMP-SMV, CoSaMp-SMV, LMMSE, AMP-MMV, and our proposed algorithm: The computational complexity versus the different parameters M_s, N_{sc}, N_{rf}, and G_rG_t.

the highly coherent, structured sensing matrix adopted in our beamspace formulation. Finally, the single-snapshot OMP-SMV and CoSaMP-SMV algorithms do not exploit any joint sparsity. Consequently, they exhibit the highest RMSE over the entire SNR range.

Fig. 8 compares the proposed pipeline against three different positioning baselines, such as a SMV based bistatic AoA and ToA based estimator, an angle-only estimator, and a delay-only estimator. These baselines are standard in localization studies because they clarify whether the performance gain originates from more reliable angle inference, more accurate delay inference, or their joint exploitation under bistatic geometry. Specifically, the proposed MMV-based method exhibits a sharp RMSE reduction as the receive SNR increases from -15 dB to -10 dB, followed by a stable error floor in the high SNR region. This behavior is expected because the proposed method estimates AoA/AoD from a discrete beamspace dictionary, and the residual angular grid mismatch dominates the high-SNR regime once the delay estimate becomes sufficiently accurate. In contrast, the SMV based method remains significantly worse across the entire SNR range. Compared to other baselines, this SMV based method does not exploit time-frequency diversity and is thus more sensitive to noise and NLoS components, which increases the probability of dominant-path mis-selection and yields biased AoA/ToA estimates. Moreover, the angle-only baseline based on three BSs improves markedly over the SMV based method and achieves a meter-level floor for SNR> -6 dB. This trend indicates that after noise becomes less dominant, the achievable accuracy is primarily limited by the angular resolution of the adopted beamspace grid. The delay-only baseline based on the ToA multilateration of 3 BSs achieves the lowest RMSE and converges close to the meter-level regime at high SNR. This improvement is mainly due to the stronger geometric observability enabled by multi-BS diversity and the averaging effect across independent ToA estimates.

Fig. 9 depicts the computational complexity evaluated from the equations in Table 3. In each subplot, only one parameter is varied while the others are fixed to $M_s = 8$, $N_{sc} = 32$, $N_{rf} = 8$, and $G_rG_t = 4 \times 10^4$. The iteration numbers are set to $T_{\text{CoSaMP}} = 5$, $T_{\text{LMMSE}} = 7$, and $T_{\text{AMP}} = 20$. In all cases the Oracle-LS benchmark exhibits the lowest complexity, since it only performs a single least–squares update over the $M_sN_{sc}N_{rf}$ unknown coefficients. The OMP-SMV and CoSaMP-SMV algorithms incur a moderate cost that is dominated by the complexity term of $\mathcal{O}(N_{rf}G_rG_t)$ and $\mathcal{O}(2T_{\text{CoSaMP}}N_{rf}G_rG_t)$, respectively. This trend prevails G is significantly higher than M_sN_{sc}, and therefore their curves remain almost flat when M_s or N_{sc} increases, while growing approximately linearly with N_{rf} and the beamspace grid size G. By contrast, the proposed joint MMV estimator, the LMMSE method and AMP-MMV all scale with

the full four-dimensional product $M_s N_{sc} N_{rf} G$, and thus their complexity increases roughly linearly with each of these parameters. Among these, the proposed scheme lies between the low-complexity greedy approaches, while the iterative methods of the LMMSE and AMP-MMV algorithms exhibit the highest complexity because each iteration requires two matrix–vector products over the entire beamspace grid. Therefore, their total cost grows proportionally with the respective number of iterations T_{LMMSE} and T_{AMP}.

V. CONCLUSION

A bistatic localization system using hybrid beamforming with a sparse MMV formulation was proposed. Specifically, a modified BOMP algorithm was conceived for recovering the angular information, while a 2D matched filter was employed for estimating the residual delay and Doppler. Furthermore, an elliptic constraint is used for recovering the UE position. The results show consistent gains for increased pilot in time- and frequency-domain, and also angular resolution. The results indicate that the proposed scheme is capable of achieving meter-level accuracy for LEO-assisted downlink localization scenarios. As an important direction for future work, it is of interest to relax the strictly orthogonal pilot allocation assumed in this paper and to investigate more general non-orthogonal pilot settings, where the resultant multi-user interference and pilot contamination must be explicitly taken into account.

REFERENCES

[1] G. Geraci, D. López-Pérez, M. Benzaghta, and S. Chatzinotas, "Integrating terrestrial and non-terrestrial networks: 3D opportunities and challenges," *IEEE Commun. Mag.*, vol. 61, no. 4, pp. 42–48, Apr. 2023.

[2] E. Erdogan, O. B. Yahia, G. K. Kurt, and H. Yanikomeroglu, "Optical HAPS eavesdropping in vertical heterogeneous networks," *IEEE Open J. Veh. Technol.*, vol. 4, pp. 208–216, 2023.

[3] J. Liang et al., "Free-space optical (FSO) satellite networks performance analysis: Transmission power, latency, and outage probability," *IEEE Open J. Veh. Technol.*, vol. 5, pp. 244–261, 2024.

[4] H. Zheng, M. Atia, and H. Yanikomeroglu, "Realistic channel and delay coefficient generation for dual mobile space-ground links: A tutorial," *IEEE Open J. Veh. Technol.*, vol. 5, pp. 762–777, 2024.

[5] H. K. Dureppagari, C. Saha, H. S. Dhillon, and R. M. Buehrer, "NTN-based 6G localization: Vision, role of LEOs, and open problems," *IEEE Wireless Commun.*, vol. 30, no. 6, pp. 44–51, Dec. 2023.

[6] K. Li, M. El-Hajjar, and L.-l. Yang, "Millimeter-wave based localization using a two-stage channel estimation relying on few-bit ADCs," *IEEE Open J. Commun. Soc.*, vol. 2, pp. 1736–1752, 2021.

[7] Z. Z. M. Kassas, J. Khalife, K. Shamaei, and J. Morales, "I hear, therefore i know where i am: Compensating for GNSS limitations with cellular signals," *IEEE Signal Process. Mag.*, vol. 34, no. 5, pp. 111–124, Sep. 2017.

[8] J. A. del Peral-Rosado, R. Raulefs, J. A. López-Salcedo, and G. Seco-Granados, "Survey of cellular mobile radio localization methods: From 1G to 5G," *IEEE Commun. Surveys Tuts.*, vol. 20, no. 2, pp. 1124–1148, Secondquarter 2018.

[9] M. Kayton, "Global positioning system: Signals, measurements, and performance [book review]," *IEEE Aerosp. Electron. Syst. Mag.*, vol. 17, no. 10, pp. 36–37, Oct. 2002.

[10] C. Zhang, Q. Li, C. Xu, L.-L. Yang, and L. Hanzo, "Space-air-ground integrated networks: Their channel model and performance analysis," *IEEE Open J. Veh. Technol.*, vol. 6, pp. 1501–1523, 2025.

[11] H. K. Dureppagari et al., "LEO-based positioning: Foundations, signal design, and receiver enhancements for 6G NTN," *IEEE Commun. Mag.*, vol. 63, no. 11, pp. 130–137, Nov. 2025.

[12] P. Angeletti and R. De Gaudenzi, "A pragmatic approach to massive MIMO for broadband communication satellites," *IEEE Access*, vol. 8, pp. 132212–132236, 2020.

[13] M. M. Azari et al., "Evolution of non-terrestrial networks from 5G to 6G: A survey," *IEEE Commun. Surveys Tuts.*, vol. 24, no. 4, pp. 2633–2672, Fourthquarter 2022.

[14] G. Araniti, A. Iera, S. Pizzi, and F. Rinaldi, "Toward 6G non-terrestrial networks," *IEEE Netw.*, vol. 36, no. 1, pp. 113–120, Jan./Feb. 2022.

[15] X. Zhu and C. Jiang, "Integrated satellite-terrestrial networks toward 6G: Architectures, applications, and challenges," *IEEE Internet Things J.*, vol. 9, no. 1, pp. 437–461, Jan. 2022.

[16] I. S. Mohamad Hashim and A. Al-Hourani, "Satellite-based localization of IoT devices using joint Doppler and angle-of-arrival estimation," *Remote Sens.*, vol. 15, no. 23, 2023, Art. no. 5603.

[17] A. K. Meshram, S. Kumar, J. Querol, and S. Chatzinotas, "Doppler effect mitigation in LEO-based 5G non-terrestrial networks," in *Proc. IEEE Globecom Workshops*, 2023, pp. 311–316.

[18] B.-H. Yeh, J.-M. Wu, and R. Y. Chang, "Efficient Doppler compensation for LEO satellite downlink OFDMA systems," *IEEE Trans. Veh. Technol.*, vol. 73, no. 12, pp. 18863–18877, Dec. 2024.

[19] L. You et al., "Integrated communications and localization for massive MIMO LEO satellite systems," *IEEE Trans. Wireless Commun.*, vol. 23, no. 9, pp. 11061–11075, Sep. 2024.

[20] M. Alsenwi, E. Lagunas, and S. Chatzinotas, "Robust beamforming for massive MIMO LEO satellite communications: A risk-aware learning framework," *IEEE Trans. Veh. Technol.*, vol. 73, no. 5, pp. 6560–6571, May 2024.

[21] J. Khalife, M. Neinavaie, and Z. M. Kassas, "Blind Doppler tracking from OFDM signals transmitted by broadband LEO satellites," in *Proc. IEEE 93rd Veh. Technol. Conf.*, 2021, pp. 1–5.

[22] D.-R. Emenonye, H. S. Dhillon, and R. Buehrer, "Fundamentals of LEO-based localization," *IEEE Trans. Inf. Theory*, vol. 71, no. 7, pp. 5277–5311, Jul. 2025.

[23] K. Li, M. El-Hajjar, and L.-L. Yang, "Reconfigurable intelligent surface aided position and orientation estimation based on joint beamforming with limited feedback," *IEEE Open J. Commun. Soc.*, vol. 4, pp. 748–767, 2023.

[24] K.-X. Li, X. Gao, and X.-G. Xia, "Channel estimation for LEO satellite massive MIMO OFDM communications," *IEEE Trans. Wireless Commun.*, vol. 22, no. 11, pp. 7537–7550, Nov. 2023.

[25] Z. Zhang et al., "User activity detection and channel estimation for grant-free random access in LEO satellite-enabled Internet of Things," *IEEE Internet Things J.*, vol. 7, no. 9, pp. 8811–8825, Sep. 2020.

[26] K. Li, J. He, M. El-Hajjar, and L.-L. Yang, "Localization in reconfigurable intelligent surface aided mmwave systems: A multiple measurement vector based channel estimation method," *IEEE Trans. Veh. Technol.*, vol. 73, no. 9, pp. 13326–13339, Sep. 2024.

[27] K. Li, M. El-Hajjar, C. Xu, and L. Hanzo, "Indoor localization and tracking in reconfigurable intelligent surface aided mmWave systems," *IEEE Open J. Veh. Technol.*, vol. 6, pp. 1815–1831, 2025.

[28] X. Wang, W. Shen, C. Xing, J. An, and L. Hanzo, "Joint Bayesian channel estimation and data detection for OTFS systems in LEO satellite communications," *IEEE Trans. Commun.*, vol. 70, no. 7, pp. 4386–4399, Jul. 2022.

[29] T. Yue, A. Liu, and X. Liang, "Block-based Kalman channel tracking for LEO satellite communication with massive MIMO," *IEEE Commun. Lett.*, vol. 27, no. 2, pp. 645–649, Feb. 2023.

[30] H. Griffiths and A. Farina, "Multistatic and networked radar: Principles and practice," in *Proc. IEEE Radar Conf.*, 2021, pp. 1–5.

[31] C. B. Barneto et al., "Full-duplex OFDM radar with LTE and 5G NR waveforms: Challenges, solutions, and measurements," *IEEE Trans. Microw. Theory Techn.*, vol. 67, no. 10, pp. 4042–4054, Oct. 2019.

[32] A. Bazzi and M. Chafii, "Low dynamic range for RIS-aided bistatic integrated sensing and communication," *IEEE J. Sel. Areas Commun.*, vol. 43, no. 3, pp. 912–927, Mar. 2025.

[33] Z. Han et al., "Cellular network based multistatic integrated sensing and communication systems," *IET Commun.*, vol. 18, no. 20, pp. 1878–1888, 2024.

[34] J. Park, J. Seong, Y. Mao, W. Shin, and B. Ottersten, "A bistatic ISAC framework for LEO satellite systems: A rate-splitting approach," *IEEE Trans. Aerosp. Electron. Syst.*, vol. 61, no. 6, pp. 17282–17301, Dec. 2025.

[35] J. Park, J. Seong, J. Ryu, Y. Mao, and W. Shin, "RSMA-based bistatic ISAC framework for LEO satellite systems," in *Proc. IEEE Int. Conf. Commun. Workshops*, 2024, pp. 1840–1845.
[36] X. Li, B. Shang, and Q. Wu, "A bistatic sensing system in space-air-ground integrated networks," in *Proc. IEEE/CIC Int. Conf. Commun. China*, 2024, pp. 1823–1827.
[37] X. Lin et al., "Doppler shift estimation in 5G new radio non-terrestrial networks," in *Proc. IEEE Glob. Commun. Conf.*, 2021, pp. 1–6.
[38] E. F. Knott, J. F. Schaeffer, and M. T. Tulley, *Radar Cross Section*. Raleigh, NC, USA: SciTech Publishing, 2004.
[39] J. Li, Y. Zhang, Y. Zhang, W. Xiong, Y. Huang, and Z. Wang, "Fast tracking doppler compensation for OFDM-based LEO satellite data transmission," in *Proc. 2nd IEEE Int. Conf. Comput. Commun*, 2016, pp. 1814–1817.
[40] L. Rothman et al., "The HITRAN2012 molecular spectroscopic database," *J. Quant. Spectrosc. Radiat. Transfer.*, vol. 130, pp. 4–50, 2013. [Online]. Available: https://www.sciencedirect.com/science/article/pii/S0022407313002859
[41] J. Jose, A. Ashikhmin, T. L. Marzetta, and S. Vishwanath, "Pilot contamination and precoding in multi-cell TDD systems," *IEEE Trans. Wireless Commun.*, vol. 10, no. 8, pp. 2640–2651, Aug. 2011.
[42] H. Yin, D. Gesbert, M. Filippou, and Y. Liu, "A coordinated approach to channel estimation in large-scale multiple-antenna systems," *IEEE J. Sel. Areas Commun.*, vol. 31, no. 2, pp. 264–273, Feb. 2013.
[43] M. Ke, Z. Gao, Y. Wu, X. Gao, and R. Schober, "Compressive sensing-based adaptive active user detection and channel estimation: Massive access meets massive MIMO," *IEEE Trans. Signal Process.*, vol. 68, pp. 764–779, 2020.
[44] K. Senel and E. G. Larsson, "Grant-free massive MTC-enabled massive MIMO: A compressive sensing approach," *IEEE Trans. Commun.*, vol. 66, no. 12, pp. 6164–6175, Dec. 2018.
[45] F. Liu et al., "Integrated sensing and communications: Toward dual-functional wireless networks for 6G and beyond," *IEEE J. Sel. Areas Commun.*, vol. 40, no. 6, pp. 1728–1767, Jun. 2022.
[46] W. Wang, T. Chen, R. Ding, G. Seco-Granados, L. You, and X. Gao, "Location-based timing advance estimation for 5G integrated LEO satellite communications," *IEEE Trans. Veh. Technol.*, vol. 70, no. 6, pp. 6002–6017, Jun. 2021.
[47] I. Matsunami, R. Nakamura, and A. Kajiwara, "RCS measurements for vehicles and pedestrian at 26 and 79GHz," in *Proc. 6th Int. Conf. Signal Process. Commun. Syst.*, 2012, pp. 1–4.
[48] G. Amendola et al., "Low-earth orbit user segment in the ku and ka-band: An overview of antennas and RF front-end technologies," *IEEE Microw. Mag.*, vol. 24, no. 2, pp. 32–48, Feb. 2023.
[49] J. A. Tropp and A. C. Gilbert, "Signal recovery from random measurements via orthogonal matching pursuit," *IEEE Trans. Inf. Theory*, vol. 53, no. 12, pp. 4655–4666, Dec. 2007.
[50] D. Needell and J. A. Tropp, "CoSaMP: Iterative signal recovery from incomplete and inaccurate samples," *Appl. Comput. Harmon. Anal.*, vol. 26, no. 3, pp. 301–321, 2009.
[51] S. Rangan, "Generalized approximate message passing for estimation with random linear mixing," in *Proc. IEEE Int. Symp. Inf. Theory*, 2011, pp. 2168–2172.
[52] L. Liu and W. Yu, "Massive connectivity with massive MIMO—Part I: Device activity detection and channel estimation," *IEEE Trans. Signal Process.*, vol. 66, no. 11, pp. 2933–2946, Jun. 2018.

KUNLUN LI (Member, IEEE) received the M.Sc and Ph.D. degrees in wireless communications from the University of Southampton, Southampton, U.K. in 2018 and 2024, respectively. He is a Research Fellow with the Next Generation Wireless Research Group, University of Southampton. His research interests include millimeter-wave, channel estimation, integrated sensing and communications (ISAC) and reconfigurable intelligent surface for wireless positioning and communications.

CHAO ZHANG (Member, IEEE) received the B.S. degree in electrical engineering from the Southwest University, China, in 2018, and the Ph.D. degree in electrical engineering from Queen Mary University of London, U.K., in 2024. He is currently a Research Fellow with the School of Electronics and Computer Science, University of Southampton, Southampton, U.K. His research interests include the channel modelling and performance analysis of stochastic-geometry-based networks, including non-orthogonal multiple access, grant-free transmission, reconfigurable intelligent surface, integrated sensing and communications, and space-air-ground integrated networks.

MOHAMMED EL-HAJJAR (Senior Member, IEEE) is a Professor of Signal Processing for Wireless Communications with the School of Electronics and Computer Science, University of Southampton, Southampton, U.K. He was the recipient of several academic awards and has published a Wiley-IEEE book and more than 150 IEEE journal and conference papers and in excess of 10 patents. His interests include the design of intelligent and energy efficient transceivers, millimeter wave communications and localisation, and machine learning for wireless communications. He is funded by the Engineering and Physical Sciences Research Council, the Royal Academy of Engineering and many industrial partners.

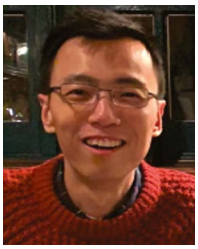

CHAO XU (Senior Member, IEEE) received the B.Eng. degree in telecommunications from Beijing University of Posts and Telecommunications, Beijing, China, the B.Sc. (Eng.) degree (with First Class Hons.) in telecommunications from the Queen Mary, University of London, London, U.K., through a Sino-U.K. joint degree Program in 2008, the M.Sc. degree (with Distinction) in radio frequency communication systems and the Ph.D. degree in wireless communications from the University of Southampton, Southampton, U.K., in 2009 and 2015, respectively. He is currently a Senior Lecturer with Next Generation Wireless Research Group, University of Southampton. His research interests include index modulation, reconfigurable intelligent surfaces, noncoherent detection, and turbo detection. He was the recipient of the Best M.Sc. Student in Broadband and Mobile Communication Networks by IEEE Communications Society United Kingdom and Republic of Ireland Chapter in 2009, 2012 Chinese Government Award for Outstanding Self-Financed Student Abroad, 2017 Dean's Award, Faculty of Physical Sciences and Engineering, University of Southampton, 2023 Marie Sklodowska-Curie Actions Global Postdoctoral Fellowships with the highest evaluation score of 100/100.

LAJOS HANZO (Life Fellow, IEEE) received the honorary doctorates from the Technical University of Budapest in 2009 and Edinburgh University in 2015. He is a Foreign Member of the Hungarian Science-Academy, Fellow of the Royal Academy of Engineering (FREng), of the IET, of EURASIP. He was the recipient of IEEE Edwin Howard Armstrong Award and IEEE Eric Sumner Technical Field Award.